

Article

Promoting Bifunctional Oxygen Catalyst Activity of Double-Perovskite-Type Cubic Nanocrystallites for Aqueous and Quasi-Solid-State Rechargeable Zinc-Air Batteries

Yijun Zhong ¹, Xiaomin Xu ¹, Chao Su ², Moses Oludayo Tadé ^{1,*} and Zongping Shao ^{1,*}

¹ WA School of Mines: Minerals, Energy and Chemical Engineering (WASM-MECE), Curtin University, Perth, WA 6102, Australia

² School of Energy and Power, Jiangsu University of Science and Technology, Zhenjiang 212100, China

* Correspondence: m.o.tade@curtin.edu.au (M.O.T.); zongping.shao@curtin.edu.au (Z.S.)

Abstract: Transition metal oxide materials are promising oxygen catalysts that are alternatives to expensive and precious metal-containing catalysts. Integration of transition metal oxides with high activity for oxygen reduction reaction (ORR) and oxygen evolution reaction (OER) is an important pathway for good bifunctionality. In contrast to the conventional physical mixing and hybridization strategies, perovskite-type oxide provides an ideal structure for the integration of the transition metal element atoms on an atomic scale. Herein, B-site ordered double-perovskite-type $\text{La}_{1.6}\text{Sr}_{0.4}\text{MnCoO}_6$ nanocrystallites with ultra-small cubic (20–50 nm) morphology and high specific surface areas ($25 \text{ m}^2 \text{ g}^{-1}$) were proposed. Rational designs were integrated to promote the ORR-OER catalysis, e.g., introducing oxygen vacancies via A-site cation substitution, further increasing surface oxygen vacancies via integration of a small amount of Pt/C and nanosizing of the material via a facile molten-salt method. The batteries with the $\text{La}_{1.6}\text{Sr}_{0.4}\text{MnCoO}_6$ nanocrystallites and an aqueous alkaline electrolyte demonstrate decent discharge–charge voltage gaps of 0.75 and 1.10 V at 1 and 30 mA cm^{-2} , respectively, and good cycling stability of 250 h (1500 cycles). A coin-type battery with a gel–polymer electrolyte also presents a good performance.



Citation: Zhong, Y.; Xu, X.; Su, C.; Tadé, M.O.; Shao, Z. Promoting Bifunctional Oxygen Catalyst Activity of Double-Perovskite-Type Cubic Nanocrystallites for Aqueous and Quasi-Solid-State Rechargeable Zinc-Air Batteries. *Catalysts* **2023**, *13*, 1332. <https://doi.org/10.3390/catal13101332>

Academic Editor: Carlo Santoro

Received: 20 August 2023

Revised: 22 September 2023

Accepted: 27 September 2023

Published: 29 September 2023



Copyright: © 2023 by the authors. Licensee MDPI, Basel, Switzerland. This article is an open access article distributed under the terms and conditions of the Creative Commons Attribution (CC BY) license (<https://creativecommons.org/licenses/by/4.0/>).

Keywords: zinc-air battery; catalyst; perovskite; nanocrystallite; solid-state battery

1. Introduction

Aqueous alkaline rechargeable Zn-air batteries represents a promising technique for large-scale electrochemical energy storage [1–4]. The sluggish kinetics of oxygen redox result in the high overpotential and relatively low energy efficiency of the Zn-air batteries. Catalysts are needed to facilitate the oxygen redox in alkaline electrolytes, i.e., ORR and OER [5,6]. An ideal catalyst for a Zn-air battery should demonstrate good bifunctional ORR-OER catalysis and should be durable for repeatably charging and discharging. Precious metals (e.g., Pt and Pd) and precious metal oxides (e.g., IrO_2 and RuO_2) have demonstrated very good catalytic activities for ORR and OER, respectively [7]. Good bifunctionality can also be easily achieved by the integration of commercial Pt/C and IrO_2 . However, most precious metals present poor cycling stability. The high costs of the precious metals also hinder their practical utility in rechargeable Zn-air batteries, especially for large-scale energy storage systems [8].

Transition metal oxide materials are promising alternatives [9,10]. Some transition metal oxides, e.g., MnO_2 , demonstrated promising catalytic activity for ORR, while some others, e.g., Co_3O_4 , showed good catalysis for OER [11,12]. Integration of transition metal oxides that takes advantage of their catalysis for either ORR or OER is an important pathway for achieving bifunctional oxygen catalysis. Conventionally, the physical mixing of different oxide materials is the simplest strategy [13]. However, this strategy may result in poor interaction between the components. Hybridization of different oxides via

a chemical or electrochemical method is another often-studied pathway [12,14,15]. This strategy, however, usually involves complicated synthesis processes or conditions, which may hinder practical utility.

Different from simple oxides, perovskite oxides are a category of cost-effective complex oxide materials that show promising catalysis in aqueous media [16]. A typical single perovskite oxide has a chemical formula of ABO_3 , where A and B are usually rare earth metal cations and transition metal cations, respectively [17]. One of the most significant advantages of perovskite oxide is its flexibility of cation element and composition. Therefore, perovskite-type oxides provide an ideal structure for the integration of the transition metal element atoms on an atomic scale, which is different from the conventional physical mixing or hybridization strategies. In addition, such integration in perovskite oxides can be easily achieved by facile one-step preparation in an ambient atmosphere, which is promising for practical production. In previous research, different single perovskite oxides (e.g., $LaNiO_3$ [18], $La_{1-x}Sr_xCo_{1-y}Mn_yO_{3-\delta}$ [19,20], $LaMn_{1-y}Co_yO_{3-\delta}$ [21], $Sr_xCo_{1-y}Fe_yO_{3-\delta}$ [22,23], $Sr(Co_{0.8}Fe_{0.2})_{0.95}P_{0.05}O_{3-\delta}$ [24]) and double perovskite oxides (e.g., Sr_2TiMnO_6 [25], $Pr_{0.5}Ba_{0.5}Mn_{1.8-x}Nb_xCo_{0.2}O_{6-\delta}$ [26], $(PrBa_{0.5}Sr_{0.5})_{0.95}Co_{1.5}Fe_{0.5}O_{5+\delta}$ [27,28]) were developed and they showed promising capability for facilitating oxygen redox as catalysts for air cathodes in Zn-air batteries [29–38].

B-site ordered double perovskite oxide is a sub-catalogue of the perovskite oxide. According to some previous reports, double perovskite demonstrates improved electrochemical stability under catalytic conditions [17,39]. Integrating two different B-site cations (e.g., Mn and Co) into the perovskite structure usually leads to a random and disordered arrangement [21]. Formation of B-site cation ordering may occur when the atomic ratio of the cations is 1:1 [17]. However, achieving the highly ordered cation arrangement is difficult and a slow growth rate is required [40]. At the same time, reducing the particle size of the catalyst can increase the specific area, which is beneficial for improving the activity due to more exposure of active sites. The molten-salt-assisted synthesis method provides an ideal route for achieving the nanosizing of the perovskite material [41,42]. Furthermore, the molten-salt environment may facilitate ionic diffusion during the synthesis process [43], which is expected to shorten the synthesis duration of the B-site ordered double perovskite.

Herein, we proposed a rationally designed B-site ordered double-perovskite-type $La_{1.6}Sr_{0.4}MnCoO_6$ nanocrystallites with an ultra-small cubic morphology and a high specific surface area for Zn-air battery cathodes. Design strategies including nanosizing of the material and introducing oxygen vacancies via A-site cation substitution to effectively improve the oxygen catalysis. A Zn-air battery with the double-perovskite-type $La_{1.6}Sr_{0.4}MnCoO_6$ nanocrystallites demonstrated good discharge–charge voltage gaps and good cycling stability. By increasing surface oxygen vacancies via the integration of a small amount of Pt/C, the bifunctional oxygen catalysis and battery performance were further promoted. This work provides new nanosizing double-perovskite-type nanocrystallites as promising bifunctional oxygen catalysts for Zn-air batteries. The molten-salt-assisted synthesis of the double-perovskite-type $La_{1.6}Sr_{0.4}MnCoO_6$ nanocrystallites will add to the knowledge base of advanced manufacturing techniques for nanosizing oxides and could inspire the development of other functional complex oxide materials.

2. Results and Discussion

2.1. Synthesis and Characterization of the Perovskite-Type Oxide Nanocrystallites

The double-perovskite-type cubic nanocrystallites (La_2MnCoO_6 , $La_{1.6}Sr_{0.4}MnCoO_6$) were prepared via a facile molten-salt process (Figure 1a). Taking $La_{1.6}Sr_{0.4}MnCoO_6$ as an example, solid solvent salt powders (Na, K nitrates) and target cation salt powders (i.e., La, Sr, Mn, Co nitrates) were dry mixed and then underwent 3 h heat treatment in an air atmosphere at 550 °C. After washing the residual solvent salts with deionized water, the double-perovskite-type cubic $La_{1.6}Sr_{0.4}MnCoO_6$ nanocrystallites were obtained.

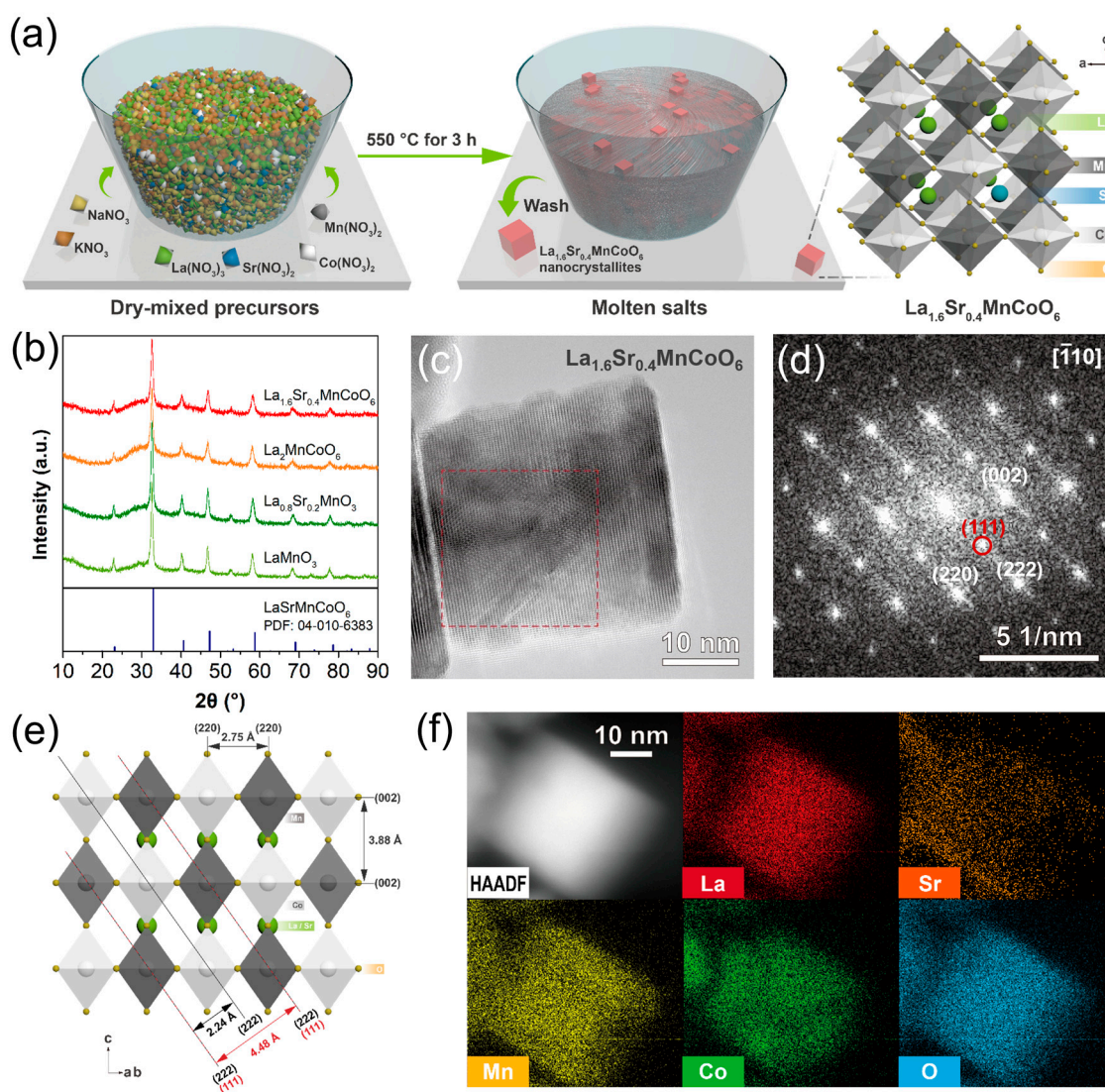


Figure 1. Synthesis and characterization of the double-perovskite-type cubic nanocrystallites. (a) Illustrative demonstration of synthesis procedure with the inset showing the atomic arrangements of $\text{La}_{1.6}\text{Sr}_{0.4}\text{MnCoO}_6$; (b) X-ray diffraction (XRD) patterns; (c) transmission electron microscopy (TEM) image; (d) corresponding fast Fourier transformed (FFT) pattern with zone axis of $[-1\ 1\ 0]$; (e) illustrative demonstration of the atomic arrangements viewed along the $[-1\ 1\ 0]$ direction; and (f) elemental mapping of a $\text{La}_{1.6}\text{Sr}_{0.4}\text{MnCoO}_6$ nanocrystallite.

The nanocrystallites show a cubic morphology with a side length of approximately 20 to 50 nm, as presented in the scanning electron microscopy (SEM, Figure S1) and TEM (Figure 1c) images. XRD patterns (Figure 1b) of the $\text{La}_2\text{MnCoO}_6$ and $\text{La}_{1.6}\text{Sr}_{0.4}\text{MnCoO}_6$ show that their phases are well aligned with a B-site (Mn and Co) ordered double perovskite with a cubic symmetry of $Fm\text{-}3m$ and a unit-cell parameter of $a \approx 7.69\ \text{\AA}$, which is double that of a cubic single perovskite (The International Centre for Diffraction Data (ICDD) database Powder Diffraction File (PDF) card No. 04-010-6383 are provided in Figure 2b as a reference) [44]. An illustration of the B-site ordered double perovskite is presented in the inset image in Figure 1a. The TEM image of a cubic $\text{La}_{1.6}\text{Sr}_{0.4}\text{MnCoO}_6$ nanocrystallite (Figure 1c) and its corresponding FFT (Figure 1d) pattern with zone axis of $[-1\ 1\ 0]$ shows the (002), (220), and (222) planes with lattice distances of 3.88, 2.75, and 2.24 Å, respectively. The pattern confirms the basic cubic structure of the material. The FFT pattern also presents a spot with weaker intensity at the position of half (222) spot. The superstructure spot represents the (111) plane with a lattice distance of 4.48 Å, which doubles

that of the (222) plane. This provides evidence that the perovskite sub-cells are doubled, which suggests the existence of the B-site ordered feature of the $\text{La}_{1.6}\text{Sr}_{0.4}\text{MnCoO}_6$ double perovskite, as illustrated in Figure 1e [44]. The high-angle annular dark-field scanning TEM (HAADF-STEM) and energy-dispersive X-ray spectroscopy (EDS) mapping images of the $\text{La}_{1.6}\text{Sr}_{0.4}\text{MnCoO}_6$ indicate the homogeneous distribution of the compositional elements (Figure 1f). Analysis of the N_2 adsorption–desorption isotherms (Figure S2) indicates that $\text{La}_2\text{MnCoO}_6$ and $\text{La}_{1.6}\text{Sr}_{0.4}\text{MnCoO}_6$ share a similar pore structure with specific areas of 22.1 and 25.2 m^2 g^{-1} and total pore volumes (micro- and mesopores) of 0.023 and 0.024 cm^3 g^{-1} , respectively (Table S1).

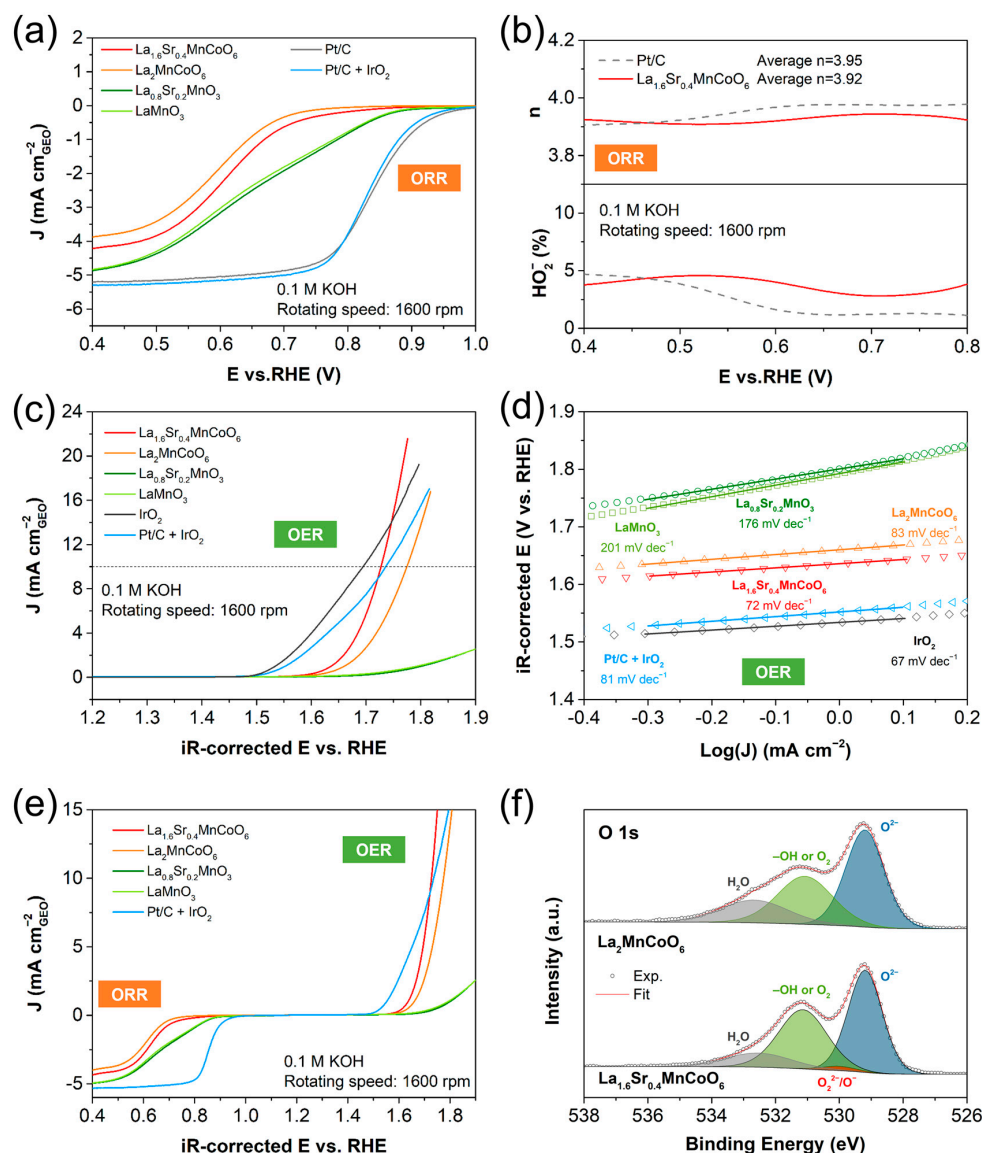


Figure 2. Bifunctional oxygen catalytic activity of the double-perovskite-type cubic nanocrystallites. (a) Comparison of ORR polarization curves for perovskite-type oxide nanocrystallites and three different commercial samples; (b) the electron transfer number (n) and HO_2^- yield percentage based on the data from rotating ring-disk electrode (RRDE). (c) Comparison of OER polarization curves for the perovskite-type materials with commercial samples and (d) corresponding Tafel plots. (e) Comparison of bifunctional oxygen catalysis activities. (f) XPS O 1s profiles of $\text{La}_2\text{MnCoO}_6$ and $\text{La}_{1.6}\text{Sr}_{0.4}\text{MnCoO}_6$ with peak fitting results.

2.2. Bifunctional Catalytic Activity for ORR and OER

The catalytic activities of ORR and OER were evaluated using a rotating disk electrode (RDE) in a 0.1 M KOH electrolyte. By integrating both Mn and Co cations into the double-perovskite-type structure, both $\text{La}_2\text{MnCoO}_6$ and $\text{La}_{1.6}\text{Sr}_{0.4}\text{MnCoO}_6$ demonstrated decent ORR-OER activity (Figure 2a,c). Without the integration of Co cations, LaMnO_3 and $\text{La}_{0.8}\text{Sr}_{0.2}\text{MnO}_3$ presented very poor catalysis for OER, though they demonstrated better catalysis for ORR (Figure 2a). The potential difference (ΔE) of major parameters, i.e., half-wave potential ($E_{1/2}$, V vs. reversible hydrogen electrode (RHE)) for ORR and potential at the current density of 10 mA cm^{-2} ($E_{j=10}$, V vs. iR-corrected RHE) for OER, is an indicator for evaluating the bifunctional catalysis. As compared in Figure 2e, the $E_{1/2}$ of $\text{La}_{1.6}\text{Sr}_{0.4}\text{MnCoO}_6$ (0.63 V) was higher than that of $\text{La}_2\text{MnCoO}_6$ (0.61 V). At the same time, the $E_{j=10}$ of $\text{La}_{1.6}\text{Sr}_{0.4}\text{MnCoO}_6$ (1.73 V) was lower than that of $\text{La}_2\text{MnCoO}_6$ (1.78 V). As a result, a decent ΔE of 1.10 V was observed for $\text{La}_{1.6}\text{Sr}_{0.4}\text{MnCoO}_6$. In addition, $\text{La}_{1.6}\text{Sr}_{0.4}\text{MnCoO}_6$ presented good selectivity of OH^- production over the unfavorable HO_2^- , which is indicated by the ~ 4 electron transfer number (Figure 2b) [45]. $\text{La}_{1.6}\text{Sr}_{0.4}\text{MnCoO}_6$ also demonstrated a Tafel slope of 72 mV dec^{-1} (Figure 2d), indicating fast OER kinetics, which is comparable to the benchmark commercial IrO_2 (67 mV dec^{-1}).

The improved catalytic activity of $\text{La}_{1.6}\text{Sr}_{0.4}\text{MnCoO}_6$ compared to $\text{La}_2\text{MnCoO}_6$ for both ORR and OER could be associated with the appearance of oxygen vacancies in the double-perovskite-type oxide, which could promote catalysis of ORR and OER according to previous reports [46,47]. Usually, oxygen vacancies are unlikely to occur in LaMnO_3 [48]. The oxygen vacancies in $\text{La}_{1.6}\text{Sr}_{0.4}\text{MnCoO}_6$ could be ascribed to the introduction of Co and the partial substitution of La (III) with Sr (II). X-ray photoelectron spectroscopy (XPS) O 1s spectra presented in Figure 2f show three main surface oxygen species: lattice oxygen (O^{2-}), hydroxide or adsorbed oxygen ($-\text{OH}^-/\text{O}_2$), and adsorbed water (H_2O) in $\text{La}_2\text{MnCoO}_6$ [49,50]. An additional peak centered at $\sim 530.1 \text{ eV}$ can be identified for $\text{La}_{1.6}\text{Sr}_{0.4}\text{MnCoO}_6$. The peak could be attributed to highly oxidative oxygen species ($\text{O}_2^{2-}/\text{O}^-$), which is related to oxygen vacancies [51,52]. The decent catalysis for ORR and OER could also be attributed to the nanosizing of the $\text{La}_{1.6}\text{Sr}_{0.4}\text{MnCoO}_6$, which results in higher surface exposure for oxygen redox. As presented in Figure S3, the $\text{La}_{1.6}\text{Sr}_{0.4}\text{MnCoO}_6$ nanocrystallites prepared via the molten-salt synthesis method demonstrated better ORR-OER activities than those of a $\text{La}_{1.6}\text{Sr}_{0.4}\text{MnCoO}_6$ sample prepared with a conventional sol-gel method, which usually produces particles with a size of several micrometers.

Although decent bifunctional catalytic activity, good selectivity of OH^- generation, and fast kinetics of OER were achieved for $\text{La}_{1.6}\text{Sr}_{0.4}\text{MnCoO}_6$, its ΔE (1.10 V) was still not comparable to that of $\text{Pt/C} + \text{IrO}_2$ (0.89 V) at this stage. Further optimization of the $\text{La}_{1.6}\text{Sr}_{0.4}\text{MnCoO}_6$ to improve its catalytic activity is required and will be demonstrated in the last section of this work.

2.3. Performance of the Zn-Air Batteries

To testify to the validation of the above analysis results, the $\text{La}_{1.6}\text{Sr}_{0.4}\text{MnCoO}_6$ nanocrystallites were applied as a catalyst on air cathodes of aqueous and quasi-solid-state Zn-air batteries. An aqueous Zn-air battery with the catalyst demonstrated a decent open-circuit voltage (OCV) of 1.44 V (Figure 3a), close to that with the $\text{Pt/C} + \text{IrO}_2$ catalyst (1.46 V). A PPD (Figure 3a) of 187 mW cm^{-2} was achieved at 419 mA cm^{-2} for $\text{La}_{1.6}\text{Sr}_{0.4}\text{MnCoO}_6$, which is comparable to that of the $\text{Pt/C} + \text{IrO}_2$ (217 mW cm^{-2} at 408 mA cm^{-2}). The high-rate performance (from 1 to 30 mA cm^{-2}) was evaluated by repeating a recharge process of 5 min galvanostatic charging and 5 min galvanostatic discharging. The median voltage points of each charging and discharging profile are presented in Figure 3b [53]. The $\text{La}_{1.6}\text{Sr}_{0.4}\text{MnCoO}_6$ cathode presented charging and discharging voltages of 2.01 and 1.26 V, respectively, indicating a decent charge-discharge voltage gap of 0.75 V, corresponding to a round-trip efficiency (i.e., voltage efficiency) of 63% at 1 mA cm^{-2} . As the overpotential increased with the rise in current densities, the voltage gaps increased to 0.82, 0.90, 0.96, 1.04, and 1.10 at 2, 5, 10, 20, and 30 mA cm^{-2} , respectively. As a comparison,

although Pt/C + IrO₂ cathode demonstrated better performance at a low current density (e.g., voltage gap of 0.62 V and voltage efficiency of 68% at 1 mA cm⁻²), the cathode experienced a fast deterioration in working voltage, especially at high current densities. The La_{1.6}Sr_{0.4}MnCoO₆ cathode also showed good voltage retention when the current density was reduced to 1 and 2 mA cm⁻², with a voltage gap of 0.73 and 0.81 V, respectively (Figure 3b).

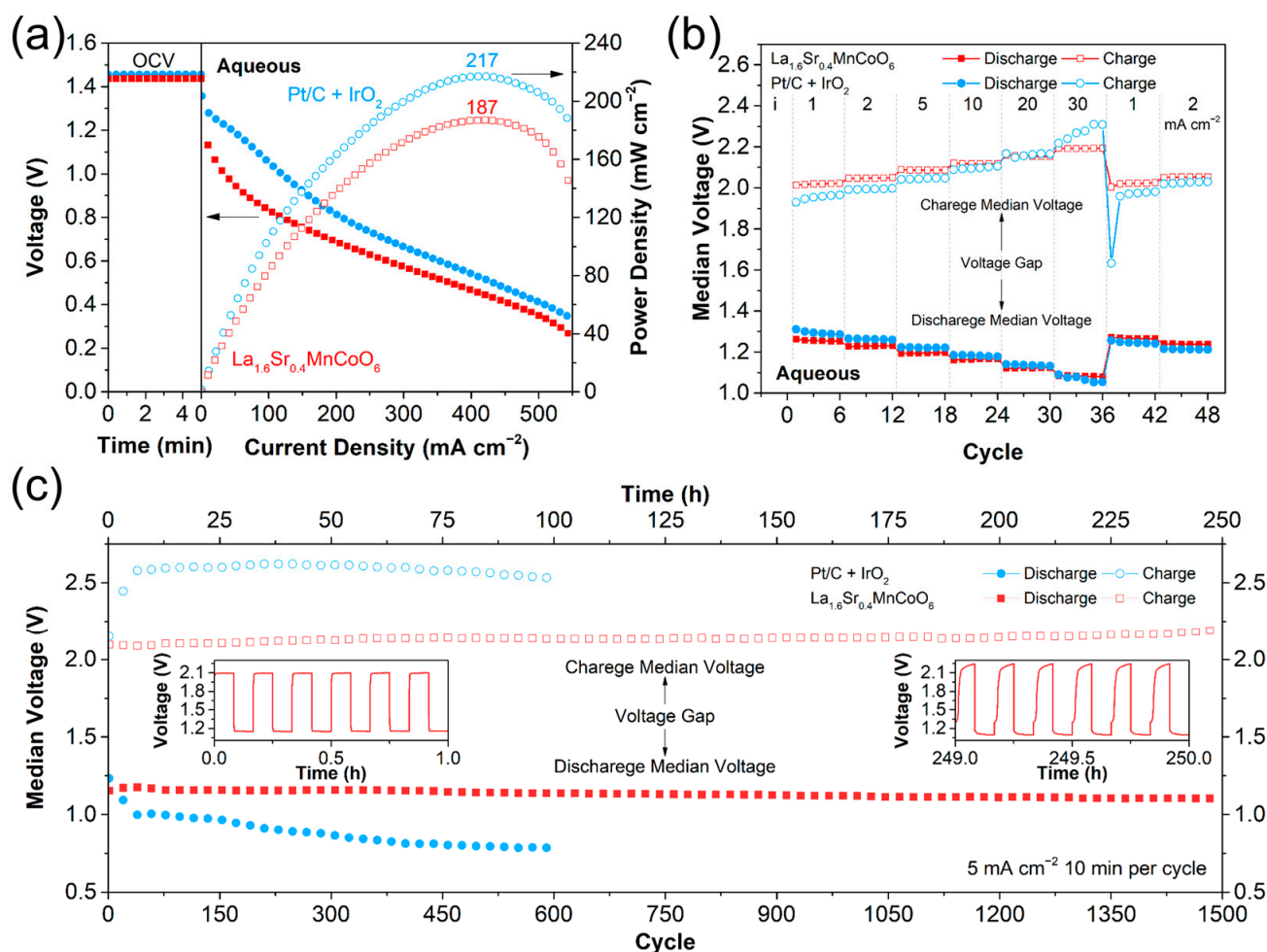


Figure 3. Performance of aqueous Zn-air batteries with a La_{1.6}Sr_{0.4}MnCoO₆ catalyst in 6 M KOH + 2 M Zn(Ac)₂ electrolyte: (a) open-circuit voltage (OCV), current density–voltage (I–V) and current density–power density (I–P) profiles with the peak power densities (PPD) annotated in the image; (b) rate performance evaluated with 5 min galvanostatic charging and 5 min galvanostatic discharging; (c) cycling stability at 5 mA cm⁻²; inset shows the specific galvanostatic charge–discharge profiles.

The battery performance of La_{1.6}Sr_{0.4}MnCoO₆ was also compared to that of La₂MnCoO₆ without Sr substitution. Benefiting from the higher ORR and OER activity, as indicated from the RDE tests presented in Figure 2, the OCV, PPD (Figure S4), and rate performance (Figure S5) of the La_{1.6}Sr_{0.4}MnCoO₆ cathode were superior to those of the La₂MnCoO₆ cathode (OCV: 1.40 V, PPD: 167 mW cm⁻²).

La_{1.6}Sr_{0.4}MnCoO₆ was also evaluated with coin-type batteries with a gel–polymer electrolyte (Figure 4a). As presented in Figure 4b, a single coin-type battery presented a decent OCV of 1.33 V and PPD of 91 mW cm⁻². The battery also showed decent cycling stability over 20 h (120 cycles), with a charge–discharge voltage gap of ~0.8 V and a round-trip efficiency of ~55% at 5 mA cm⁻² (Figure 4c). A three-series coin-type battery group was also established to verify the practical utility of powering small electronic devices. The

battery group presented an OCV of 3.94 V, which dropped to 2.60 V when 21 light-emitting diode (LED) bulbs were lit (Figure 4d). Once the work loading was removed, the voltage quickly recovered to a level (3.79 V) close to the original OCV within 10 s.

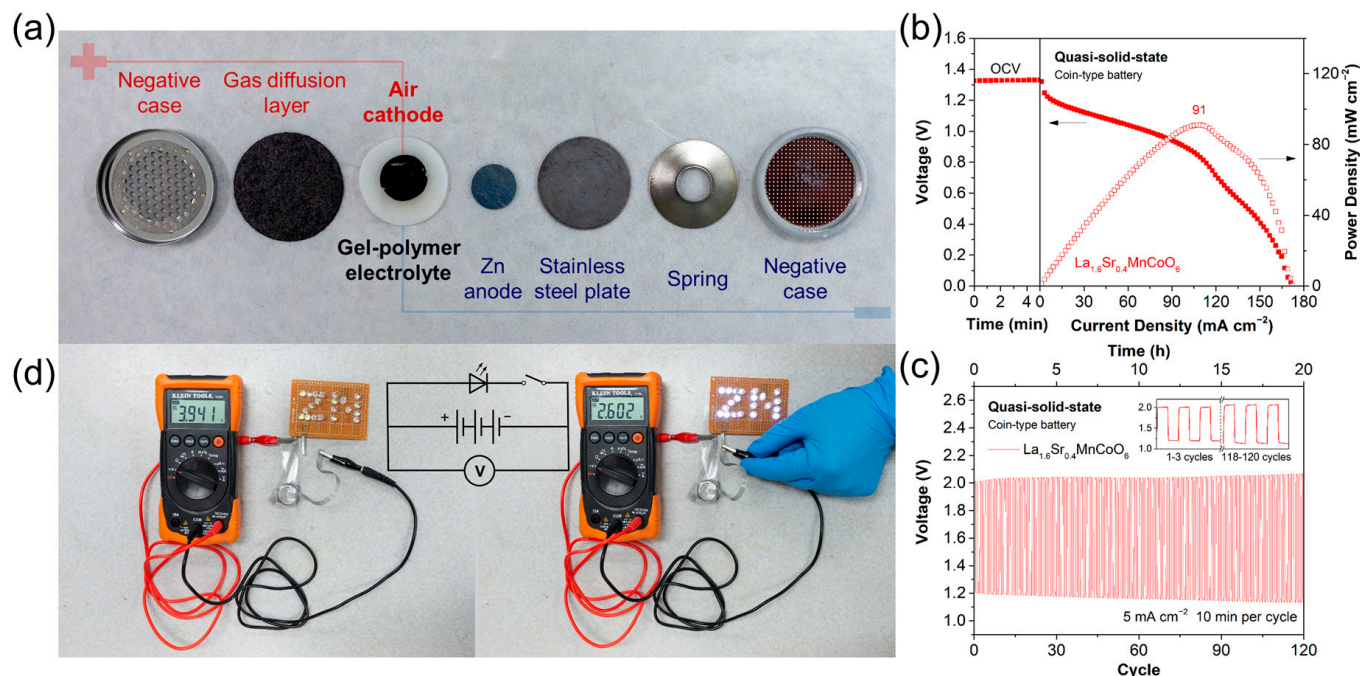


Figure 4. Performance of coin-type quasi-solid-state Zn-air battery. (a) Configuration of the coin-type quasi-solid-state Zn-air battery, (b) OCV, I-V, and I-P profiles with the PPD annotated in the image, (c) cycling stability evaluation at 5 mA cm^{-2} , (d) OCV of a three-series coin-type battery group and working voltage for lighting 21 LED bulbs in parallel.

As presented in Figure 3c, the $\text{La}_{1.6}\text{Sr}_{0.4}\text{MnCoO}_6$ cathode also demonstrated superior stability (compared to the commercial Pt/C + IrO_2 catalyst) in 1500 recharging cycles (250 h) at 5 mA cm^{-2} . During the cycling performance, the $\text{La}_{1.6}\text{Sr}_{0.4}\text{MnCoO}_6$ cathode showed a gradual increase in voltage gap (inset image in Figure 3c) from 0.95 V (1st cycle) to 1.09 V (1500th cycle). The stability was much better than that of the Pt/C + IrO_2 cathode, which presented a significant increase of overpotentials after cycling for only a few hours. Prolonged cycling of the Zn-air battery over 333 h (1000 cycles) was conducted to evaluate the stability of the $\text{La}_{1.6}\text{Sr}_{0.4}\text{MnCoO}_6$ material and identify the potential reason for the degradation of battery performance. As presented in Figure S6a, a significant increase in overpotentials for both charging and discharging was observed. The Zn-air battery after cycling for 333 h was disassembled and the $\text{La}_{1.6}\text{Sr}_{0.4}\text{MnCoO}_6$ cathode was characterized by XRD (Figure S6b), where a cathode before cycling and a cathode after cycling for 50 h were also compared. The characteristic perovskite-type crystal structure remains for the cathode after testing for 50 and 333 h. This indicates the good stability of the crystal structure of $\text{La}_{1.6}\text{Sr}_{0.4}\text{MnCoO}_6$, which is beneficial to the stable running of the battery. The fast performance degradation after 250 h could be associated with the precipitation of inert ZnO in the cathode, which could be associated with the over-saturation of zincate ion after prolonged cycling due to the accumulation of product from the irreversible redox of the Zn anode [54,55], which was evidenced by the XRD result presented in Figure S6b. The accumulation of ZnO deposition could result in the deterioration of gas and ionic transfer pathways.

2.4. Integration of a Small Amount of Pt/C for Optimization of Oxygen Catalysis

The decent performance and very good stability presented above suggest that the double-perovskite-type $\text{La}_{1.6}\text{Sr}_{0.4}\text{MnCoO}_6$ is a promising bifunctional oxygen catalyst for

practical Zn-air batteries. As discussed in the last few sections, the oxygen vacancies introduced by the Sr doping were the origin of the enhanced catalytic activity (Figure 5d). Sr doping is a modification of the entire bulk particles, and the oxygen vacancies may disperse on both the particle bulk and surface. Moreover, the substitution amount of Sr has a limitation which is restricted by the perovskite structure itself. It is worth noting that OER and ORR are usually more likely to happen on the catalyst surface. To further increase surface oxygen vacancies, a facile Pt/C decoration strategy was introduced (Figure S7). Commercial Pt/C was physically mixed with the $\text{La}_{1.6}\text{Sr}_{0.4}\text{MnCoO}_6$ using an ultrasonic bath. Even though the mass ratio of Pt/C to the perovskite was controlled at a very low value (2 to 5 wt% of Pt to $\text{La}_{1.6}\text{Sr}_{0.4}\text{MnCoO}_6$), the ORR and OER activity was significantly boosted. As presented in Figure 5a, the $\text{La}_{1.6}\text{Sr}_{0.4}\text{MnCoO}_6$ -Pt mixture with a Pt loading of 2% and 5% demonstrated a ΔE (based on RDE test in 0.1 M KOH) of 0.90 and 0.85 V (vs. iR-corrected RHE), which is highly superior to that without Pt decoration (1.10 V). This improvement in the bifunctional catalysis was also reflected by the galvanostatic charging–discharging performance of the Zn-air battery (with 6 M KOH + 0.2 M $\text{Zn}(\text{Ac})_2$). As compared in Figure 5b, a decrease in voltage gaps (0.95, 0.88, 0.85 V vs. Zn) and an increase in round-trip efficiency (55%, 58%, 59%) were observed for samples with the introduction of 0%, 2%, and 5% Pt. The XPS O 1s spectra (Figure 5c) indicated the increased amount of $\text{O}_2^{2-}/\text{O}^-$, which is highly related to surface oxygen vacancy for the samples with Pt decoration (Pt 4f spectra supplemented in Figure S8) [51]. This could be associated with the surface charge transfer from Pt/C to cation elements in the $\text{La}_{1.6}\text{Sr}_{0.4}\text{MnCoO}_6$, which results in the formation of more oxygen vacancies on the perovskite surface as compensation (Figure 5e) [24].

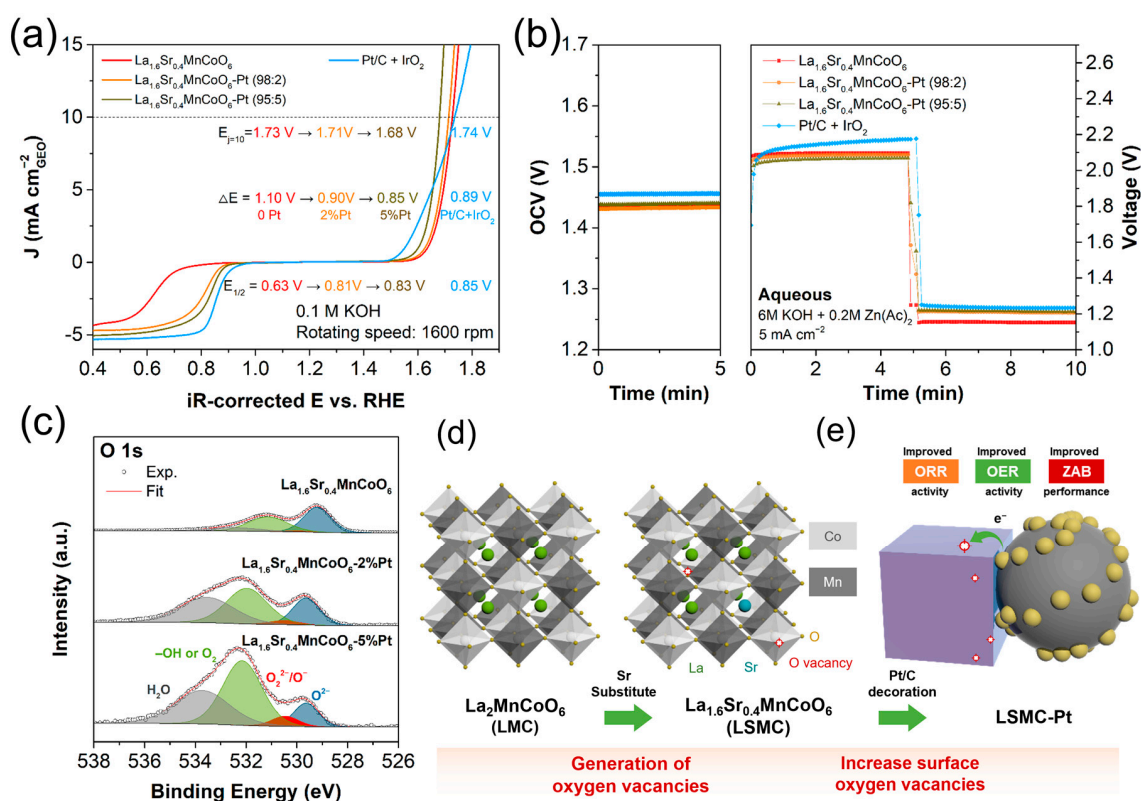


Figure 5. Further optimization of the oxygen catalysis. Comparison of (a) bifunctional oxygen catalysis activities and (b) OCV and first discharge–charge cycle at 5 mA cm⁻² of Zn-air battery, and (c) XPS O 1s spectra of $\text{La}_{1.6}\text{Sr}_{0.4}\text{MnCoO}_6$ and Pt/C decorated $\text{La}_{1.6}\text{Sr}_{0.4}\text{MnCoO}_6$ samples. Illustrative demonstration that the improvement in bifunctional oxygen catalysis activity benefited from (d) generation of oxygen vacancies via partial Sr substitution in the perovskite structure and (e) increased surface oxygen vacancies induced by facile Pt/C decoration.

3. Experimental Section

3.1. Synthesis of Perovskite-Type Oxide Nanocrystallites

A fast and low-temperature synthesis of perovskite-type oxide nanocrystallites was achieved using Na-K nitrate molten salts as a highly oxidized medium, which was adjusted based on the method reported by Tian et al. [42] La, Sr, Mn, and Co nitrate salts were utilized as the source of the cations and the amount of each cation was determined according to the stoichiometric number of the target perovskite products. Taking the synthesis of 0.005 mol $\text{La}_{1.6}\text{Sr}_{0.4}\text{MnCoO}_6$ as an example, 3.46 g $\text{La}(\text{NO}_3)_3 \cdot 6\text{H}_2\text{O}$, 0.42 g $\text{Sr}(\text{NO}_3)_2$, 1.26 g $\text{Mn}(\text{NO}_3)_2 \cdot 4\text{H}_2\text{O}$, and 1.46 g $\text{Co}(\text{NO}_3)_2 \cdot 6\text{H}_2\text{O}$ (weights calculated based on the stoichiometric ratio of cations in $\text{La}_{1.6}\text{Sr}_{0.4}\text{MnCoO}_6$) were manually dry-mixed in a mortar for 5 min. The molar ratio of the above cation elements was La:Sr:Mn:Co = 8:2:5:5, and the total molar amount of the cation was 0.02 mol. After that, pre-mixed salts consisting of 5.67 g NaNO_3 and 3.37 g of KNO_3 (the total molar amount of Na + K was 0.1 mol) were added and further milled for 5 min. The resulting pink-colored powder was then transferred into a crucible and heated at 550 °C for 3 h (heating rate 10 °C min^{-1}). After the crucible was cooled, 80 mL DI water was added into the crucible and put into an ultrasonic bath for 10 min to dissolve the rigid nitrate salts. The resulting dispersion was vacuum filtered, and then repeatedly washed with DI water three additional times. The washed powder was dried at 60 °C.

For comparison, a $\text{La}_{1.6}\text{Sr}_{0.4}\text{MnCoO}_6$ bulk particle sample was prepared via a conventional sol–gel method. As is typical, 3.46 g $\text{La}(\text{NO}_3)_3 \cdot 6\text{H}_2\text{O}$, 0.42 g $\text{Sr}(\text{NO}_3)_2$, 1.26 g $\text{Mn}(\text{NO}_3)_2 \cdot 4\text{H}_2\text{O}$, and 1.46 g $\text{Co}(\text{NO}_3)_2 \cdot 6\text{H}_2\text{O}$ were dissolved in 100 mL of deionized water. Quantities of 5.84 g of ethylenediaminetetraacetic acid (EDTA), 7.68 g citric acid (CA), and 15.5 mL ammonia solution were added to the solution. The mixture was heated at 180 °C until a transparent gel was formed. Then the gel was heated at 250 °C for 5 h. The obtained precursor was further calcinated at 700 °C for 5 h.

3.2. Material Characterizations

Morphologies of the double-perovskite-type cubic nanocrystallites were observed using microscopic techniques including SEM (Zeiss Neon) and TEM (Titan G2). Crystal structures of the samples were analyzed using XRD (Bruker D8 Advance, Cu $K\alpha$ radiation) and high-resolution TEM (HR-TEM, Titan G2). Dispersion of the cations was evaluated using the EDS mapping technique via the Titan G2 TEM. The composition ratio of the cations was evaluated by the EDS system (Oxford) equipped with an SEM (Tescan Clara). Porosity information of the materials was analyzed using the 77 K liquid nitrogen adsorption–desorption technique (Micromeritics TriStar). The chemical state of elements on the perovskite surface was analyzed using XPS (Al $K\alpha$ radiation).

3.3. Evaluation of Oxygen Catalytic Activity

As a common practice for evaluating the catalytic activity of perovskite oxide [16,51], the oxide materials were mixed with conductive carbon (i.e., Super P), which ensures sufficient electrical conductivity on the RDE. A dispersion consisting of 10 mg oxide, 10 mg Super P, 1 mL ethanol, and 100 μL Nafion[®]117 solution (5 wt%) was made and 5 μL of the dispersion was drop-cast on the glassy carbon area of a RDE (weight loading of the oxide catalyst: $\sim 0.232 \text{ mg cm}^{-2}$). Commercial Pt/C and IrO_2 were also evaluated for comparisons. The same electrode dispersion composition as that containing perovskites was adopted for the IrO_2 sample (10 mg of IrO_2 , 10 mg of Super P), while no additional Super P was added for the 20% Pt/C sample (10 mg of 20% Pt/C). For the Pt/C + IrO_2 mixture sample, 5 mg 20% Pt/C, 5 mg IrO_2 , and 10 mg Super P were applied.

Electrochemical measurements for evaluating the oxygen catalytic activity were carried out using the RDE in a three-electrode cell with Pt wire as the counter electrode, Ag/AgCl (4 M KCl) as the reference electrode, and 0.1 M KOH aqueous solution as the electrolyte. The electrolyte was purged with O_2 for 30 min before the test and purging continued during the test. The electrochemical evaluation was conducted with a potentiostat (CHI760E).

Linear sweep voltammetry (LSV) with a scan rate of 5 mV s^{-1} was performed at 1600 rpm. The voltages from the RDE curves are presented in RHE, converted with the equation: $E(\text{RHE}) = E(\text{Ag}/\text{AgCl}) + 0.199 + 0.0591 \times \text{pH}$. Ohmic voltage drop was considered with a resistance ($\sim 45 \Omega$) of the working electrode.

An RRDE (Pine Instruments AFE7R9GCPT) was utilized to evaluate the electron transfer number (n). The ping potential was settled at 0.5 V (vs. Ag/AgCl). The value of n and percentage of HO_2^- in the total reduced product (X) was calculated using the equations below:

$$n = 4 \times \frac{I_d}{I_d + I_r/N}$$

$$X = 200 \times \frac{I_r/N}{I_d + I_r/N}$$

I_d : disk current, I_r : ring current, N : current efficiency = 37%

For the $\text{La}_{1.6}\text{Sr}_{0.4}\text{MnCoO}_6$ catalyst sample with a small amount (2–5 wt%) of Pt/C, the mass loading of oxide and metallic Pt on the working electrode was the same as that without Pt/C ($\sim 0.232 \text{ mg cm}^{-2}$), and the ratio of oxide + Pt to carbon was fixed at 1:1. Taking $\text{La}_{1.6}\text{Sr}_{0.4}\text{MnCoO}_6$ -Pt (95:5) as an example, the electrode dispersion consists of 9.5 mg oxide, 2.5 mg commercial 20% Pt/C (containing 0.5 mg Pt and 2 mg carbon support), 8 mg Super P, 1 mL ethanol, and 100 μL Nafion solution. To ensure the accuracy of weighing, 10 times the above weighting of the oxide, commercial 20% Pt/C, and Super P were premixed in 10 mL ethanol in an ultrasonic bath and dried at 60°C . Then, 1/10 of the weighting amount of the mixture (20 mg) was used for preparing the dispersion.

3.4. Evaluation of Aqueous Zn-Air Batteries

Typically, 55 μL of the catalyst dispersion (the same composition as that for the RDE test, which contains 0.5 mg oxide) was drop-cast on $15 \times 15 \text{ mm}$ hydrophobic carbon paper (AVCarb P75T) within a $\phi 8 \text{ mm}$ circular coated area ($\sim 0.5 \text{ cm}^2$, oxide loading of 1 mg cm^{-2}). After drying at 100°C to evaporate the ethanol, the air cathode film was placed in the positive side of a homemade Zn-air battery model. A Zn plate was placed in the negative side and 2 mL 6 M KOH + 0.2 M $\text{Zn}(\text{Ac})_2$ electrolyte was injected into the chamber between the positive and negative electrodes. OCV, I-V, and I-P profiles, and PPD of the aqueous Zn-air batteries were evaluated using a potentiostat (Biologic VSP). Galvanostatic cycling was evaluated using a battery tester (LANHE CT2001A).

3.5. Evaluation of Coin-Type Zn-Air Batteries with Gel–Polymer Electrolyte

SiO_2 nanoparticle-modified polyvinyl alcohol (PVA)-based gel–polymer electrolyte was prepared using a cast and freeze method. As is typical, 25 g DI water and 2.5 g PVA were mixed at 100°C , followed by adding 0.83 g SiO_2 dispersion (containing 0.25 g nano SiO_2) at 100°C until a high-viscosity mixture with evenly dispersed SiO_2 nanoparticles was formed. The mixture was cast in a coin-type CR2016 positive battery case. A freezing (-20°C , 24 h) and unfreezing (room temperature, 2 h) process was repeated 2 times until the cast mixture eventually formed a flexible and stretchable gel. The gel film was removed from the CR2016 case and soaked in a 1 M KOH + 0.2 M $\text{Zn}(\text{Ac})_2$ solution for 24 h. As presented in Figure 4d, a coin-type quasi-solid-state Zn-air battery was assembled according to the following order: (1) a meshed CR2032 negative case, (2) a piece of $\phi 19 \text{ mm}$ hydrophobic carbon paper as a gas diffusion layer, (3) a $\phi 8 \text{ mm}$ catalyst film (perovskite:CNT:PTFE = 6:2:2 wt:wt:wt), (4) a gel–polymer electrolyte film, (5) a $\phi 8 \text{ mm}$ Zn plate as an anode, (6) a $\phi 16 \text{ mm}$ stainless steel plate, (7) a stainless steel spring, and (8) a CR2032 negative case.

4. Conclusions

In conclusion, rational designs including introducing and increasing oxygen vacancies and nanosizing of the B-site ordered double perovskite were proposed to effectively

improve the bifunctional oxygen catalysis. The B-site ordered double-perovskite-type nanocrystallites with ultra-small cubic (20–50 nm length) morphology and high specific surface areas ($25 \text{ m}^2 \text{ g}^{-1}$) were prepared via a molten-salt method. Due to the introduction of the oxygen vacancies via partial substitution of La with Sr, the $\text{La}_{1.6}\text{Sr}_{0.4}\text{MnCoO}_6$ nanocrystallites demonstrated improved catalytic activity for both ORR and OER. Zn-air batteries with the $\text{La}_{1.6}\text{Sr}_{0.4}\text{MnCoO}_6$ as an oxygen catalyst demonstrated decent discharge–charge voltage gaps of 0.75 and 1.10 V at 1 and 30 mA cm^{-2} , respectively, and good cycling stability for more than 250 h with a fair voltage gap of $\sim 1\text{V}$ in an alkaline electrolyte. The crystal structure of the $\text{La}_{1.6}\text{Sr}_{0.4}\text{MnCoO}_6$ nanocrystallites remained stable after hundreds of hours of charge–discharge cycling. A coin-type Zn-air battery with the $\text{La}_{1.6}\text{Sr}_{0.4}\text{MnCoO}_6$ and an alkaline gel–polymer electrolyte also presented good performance and decent stability. Further enhancement of the ORR–OER catalysis and performance of the Zn-air battery was achieved by increasing surface oxygen vacancies via integrating a small amount of Pt on the surface of $\text{La}_{1.6}\text{Sr}_{0.4}\text{MnCoO}_6$.

Supplementary Materials: The following supporting information can be downloaded at: <https://www.mdpi.com/article/10.3390/catal13101332/s1>, Figure S1: SEM images of (a), (b) $\text{La}_2\text{MnCoO}_6$ and (c), (d) $\text{La}_{1.6}\text{Sr}_{0.4}\text{MnCoO}_6$ nanocrystallites; Figure S2: N_2 adsorption-desorption isotherms of the perovskite-type nanocrystallites; Table S1: Physical parameters for the perovskite-type nanocrystallites; Figure S3: Comparison of (a) ORR and (b) OER polarization curves of $\text{La}_{1.6}\text{Sr}_{0.4}\text{MnCoO}_6$ nanocrystallites synthesized via a molten-salt method and $\text{La}_{1.6}\text{Sr}_{0.4}\text{MnCoO}_6$ particle synthesized via a sol-gel method; Figure S4. Comparison of OCV, I-V and I-P profiles with PPD annotated in the image for aqueous Zn-air batteries with $\text{La}_2\text{MnCoO}_6$ or $\text{La}_{1.6}\text{Sr}_{0.4}\text{MnCoO}_6$ as the catalyst; Figure S5: Comparison of rate performance for aqueous Zn-air batteries with $\text{La}_2\text{MnCoO}_6$ or $\text{La}_{1.6}\text{Sr}_{0.4}\text{MnCoO}_6$ as air cathode with 10-minute galvanostatic charging-discharging cycles; Figure S6: (a) A prolonged 2000-cycle (~ 333 h) test until build-up of overpotential of aqueous Zn-air battery with a $\text{La}_{1.6}\text{Sr}_{0.4}\text{MnCoO}_6$ as air cathode; (b) XRD profiles of the initial $\text{La}_{1.6}\text{Sr}_{0.4}\text{MnCoO}_6$ as air cathode and after 50 h and 333 h; Figure S7: SEM images of (a) $\text{La}_{1.6}\text{Sr}_{0.4}\text{MnCoO}_6\text{-Pt}$ (98:2) and (b) $\text{La}_{1.6}\text{Sr}_{0.4}\text{MnCoO}_6\text{-Pt}$ (95:5) and (c) EDS profiles; Figure S8: XPS Pt 4f spectra of Pt/C, $\text{La}_{1.6}\text{Sr}_{0.4}\text{MnCoO}_6\text{-Pt}$ (98:2) and $\text{La}_{1.6}\text{Sr}_{0.4}\text{MnCoO}_6\text{-Pt}$ (95:5); Table S2: Comparison of physical parameters of some representative catalysts and performances of aqueous Zn–air batteries [3,19,24,25,56,57].

Author Contributions: Conceptualization, Y.Z. and Z.S.; methodology, Y.Z., X.X. and C.S.; validation, Y.Z., M.O.T. and Z.S.; formal analysis, Y.Z. and X.X.; investigation, Y.Z.; data curation, Y.Z.; writing—original draft preparation, Y.Z.; writing—review and editing, Y.Z., X.X., C.S., M.O.T. and Z.S.; visualization, Y.Z.; supervision, C.S., M.O.T. and Z.S.; project administration, M.O.T. and Z.S.; funding acquisition, M.O.T. and Z.S. All authors have read and agreed to the published version of the manuscript.

Funding: This research was supported by the Australian Research Council Discovery Projects, Grant Nos. DP200103332, DP200103315 and DP220103669.

Data Availability Statement: All the relevant data are included in this published article.

Acknowledgments: Part of this research was undertaken using the SEM, XRD, XPS instrumentation (ARC LE0775553, LE0775551, LE120100026) at the John de Laeter Centre, Curtin University. The authors acknowledge the TEM facilities, and the scientific and technical assistance of the Australian National Fabrication Facility at the Centre for Microscopy, Characterization & Analysis, The University of Western Australia, a facility funded by the University, State and Commonwealth Governments.

Conflicts of Interest: The authors declare no conflict of interest.

References

1. Li, Y.; Lu, J. Metal Air Batteries: Will They Be the Future Electrochemical Energy Storage Device of Choice? *ACS Energy Lett.* **2017**, *2*, 1370–1377. [[CrossRef](#)]
2. Fu, J.; Cano, Z.P.; Park, M.G.; Yu, A.; Fowler, M.; Chen, Z. Electrically Rechargeable Zinc-Air Batteries: Progress, Challenges, and Perspectives. *Adv. Mater.* **2017**, *29*, 1604685. [[CrossRef](#)] [[PubMed](#)]
3. Arafat, Y.; Azhar, M.R.; Zhong, Y.; Abid, H.R.; Tade, M.O.; Shao, Z. Advances in Zeolite Imidazolate Frameworks (ZIFs) Derived Bifunctional Oxygen Electrocatalysts and Their Application in Zinc–Air Batteries. *Adv. Energy Mater.* **2021**, *11*, 2100514. [[CrossRef](#)]

4. Zhu, Z.; Jiang, T.; Ali, M.; Meng, Y.; Jin, Y.; Cui, Y.; Chen, W. Rechargeable Batteries for Grid Scale Energy Storage. *Chem. Rev.* **2022**, *122*, 16610–16751. [[CrossRef](#)] [[PubMed](#)]
5. Cai, X.; Lai, L.; Lin, J.; Shen, Z. Recent Advances in Air Electrodes for Zn-Air Batteries: Electrocatalysis and Structural Design. *Mater. Horiz.* **2017**, *4*, 945–976. [[CrossRef](#)]
6. Zhong, Y.; Xu, X.; Wang, W.; Shao, Z. Recent Advances in Metal-Organic Framework Derivatives as Oxygen Catalysts for Zinc-Air Batteries. *Batter. Supercaps* **2019**, *2*, 272–289. [[CrossRef](#)]
7. Huang, Y.; Wang, Y.; Tang, C.; Wang, J.; Zhang, Q.; Wang, Y.; Zhang, J. Atomic Modulation and Structure Design of Carbons for Bifunctional Electrocatalysis in Metal-Air Batteries. *Adv. Mater.* **2019**, *31*, 1803800. [[CrossRef](#)]
8. Han, C.; Li, W.; Liu, H.-K.; Dou, S.; Wang, J. Design Strategies for Developing Non-Precious Metal Based Bi-Functional Catalysts for Alkaline Electrolyte Based Zinc–Air Batteries. *Mater. Horiz.* **2019**, *6*, 1812–1827. [[CrossRef](#)]
9. Hong, W.T.; Risch, M.; Stoerzinger, K.A.; Grimaud, A.; Suntivich, J.; Shao-Horn, Y. Toward the Rational Design of Non-Precious Transition Metal Oxides for Oxygen Electrocatalysis. *Energy Environ. Sci.* **2015**, *8*, 1404–1427. [[CrossRef](#)]
10. Cao, R.; Lee, J.-S.; Liu, M.; Cho, J. Recent Progress in Non-Precious Catalysts for Metal-Air Batteries. *Adv. Energy Mater.* **2012**, *2*, 816–829. [[CrossRef](#)]
11. Pan, J.; Tian, X.L.; Zaman, S.; Dong, Z.; Liu, H.; Park, H.S.; Xia, B.Y. Recent Progress on Transition Metal Oxides as Bifunctional Catalysts for Lithium-Air and Zinc-Air Batteries. *Batter. Supercaps* **2019**, *2*, 336–347. [[CrossRef](#)]
12. Du, G.; Liu, X.; Zong, Y.; Hor, T.S.A.; Yu, A.; Liu, Z. Co₃O₄ Nanoparticle-Modified MnO₂ Nanotube Bifunctional Oxygen Cathode Catalysts for Rechargeable Zinc-Air Batteries. *Nanoscale* **2013**, *5*, 4657–4661. [[CrossRef](#)] [[PubMed](#)]
13. Ma, H.; Wang, B. A Bifunctional Electrocatalyst α -MnO₂-LaNiO₃/Carbon Nanotube Composite for Rechargeable Zinc-Air Batteries. *RSC Adv.* **2014**, *4*, 46084–46092. [[CrossRef](#)]
14. Xu, N.; Liu, Y.; Zhang, X.; Li, X.; Li, A.; Qiao, J.; Zhang, J. Self-Assembly Formation of Bi-Functional Co₃O₄/MnO₂-CNTs Hybrid Catalysts for Achieving Both High Energy/Power Density and Cyclic Ability of Rechargeable Zinc-Air Battery. *Sci. Rep.* **2016**, *6*, 33590. [[CrossRef](#)]
15. Luo, Z.; Irtem, E.; Ibanez, M.; Nafria, R.; Marti-Sanchez, S.; Genc, A.; de la Mata, M.; Liu, Y.; Cadavid, D.; Llorca, J.; et al. Mn₃O₄@CoMn₂O₄-Co_xO_y Nanoparticles: Partial Cation Exchange Synthesis and Electrocatalytic Properties toward the Oxygen Reduction and Evolution Reactions. *ACS Appl. Mater. Interfaces* **2016**, *8*, 17435–17444. [[CrossRef](#)] [[PubMed](#)]
16. Xu, X.; Wang, W.; Zhou, W.; Shao, Z. Recent Advances in Novel Nanostructuring Methods of Perovskite Electrocatalysts for Energy-Related Applications. *Small Methods* **2018**, *2*, 1800071. [[CrossRef](#)]
17. Xu, X.; Zhong, Y.; Shao, Z. Double Perovskites in Catalysis, Electrocatalysis, and Photo(electro)catalysis. *Trends Chem.* **2019**, *1*, 410–424. [[CrossRef](#)]
18. Chen, Z.; Yu, A.; Higgins, D.; Li, H.; Wang, H.; Chen, Z. Highly Active and Durable Core-Corona Structured Bifunctional Catalyst for Rechargeable Metal-Air Battery Application. *Nano Lett.* **2012**, *12*, 1946–1952. [[CrossRef](#)]
19. Wang, Q.; Xue, Y.; Sun, S.; Li, S.; Miao, H.; Liu, Z. La_{0.8}Sr_{0.2}Co_{1-x}Mn_xO₃ Perovskites as Efficient Bi-Functional Cathode Catalysts for Rechargeable Zinc-Air Batteries. *Electrochim. Acta* **2017**, *254*, 14–24. [[CrossRef](#)]
20. Dai, Y.; Yu, J.; Zhang, Z.; Zhai, S.; Cheng, C.; Zhao, S.; Tan, P.; Shao, Z.; Ni, M. Regulating the Interfacial Electron Density of La_{0.8}Sr_{0.2}Mn_{0.5}Co_{0.5}O₃/RuO_x for Efficient and Low-Cost Bifunctional Oxygen Electrocatalysts and Rechargeable Zn-Air Batteries. *ACS Appl. Mater. Interfaces* **2021**, *13*, 61098–61106. [[CrossRef](#)]
21. Bian, J.; Li, Z.; Li, N.; Sun, C. Oxygen Deficient LaMn_{0.75}Co_{0.25}O_{3- δ} Nanofibers as an Efficient Electrocatalyst for Oxygen Evolution Reaction and Zinc-Air Batteries. *Inorg. Chem.* **2019**, *58*, 8208–8214. [[CrossRef](#)] [[PubMed](#)]
22. Park, H.W.; Lee, D.U.; Zamani, P.; Seo, M.H.; Nazar, L.F.; Chen, Z. Electrospun Porous Nanorod Perovskite Oxide/Nitrogen-Doped Graphene Composite as a Bi-Functional Catalyst for Metal Air Batteries. *Nano Energy* **2014**, *10*, 192–200. [[CrossRef](#)]
23. Xu, X.; Pan, Y.; Zhong, Y.; Shi, C.; Guan, D.; Ge, L.; Hu, Z.; Chin, Y.-Y.; Lin, H.-J.; Chen, C.-T.; et al. New Undisputed Evidence and Strategy for Enhanced Lattice-Oxygen Participation of Perovskite Electrocatalyst through Cation Deficiency Manipulation. *Adv. Sci.* **2022**, *9*, 2200530. [[CrossRef](#)]
24. Wang, X.; Sunarso, J.; Lu, Q.; Zhou, Z.; Dai, J.; Guan, D.; Zhou, W.; Shao, Z. High-Performance Platinum-Perovskite Composite Bifunctional Oxygen Electrocatalyst for Rechargeable Zn-Air Battery. *Adv. Energy Mater.* **2020**, *10*, 1903271. [[CrossRef](#)]
25. Bhardwaj, U.; Sharma, A.; Mathur, A.; Halder, A.; Kushwaha, H.S. Synthesis of a Novel Sr₂TiMnO₆ Double Perovskite Electrocatalyst for Rechargeable Zinc–Air Batteries. *Energy Storage* **2022**, *4*, e293. [[CrossRef](#)]
26. Mondal, S.; Majee, R.; Arif Islam, Q.; Bhattacharyya, S. 2D Heterojunction Between Double Perovskite Oxide Nanosheet and Layered Double Hydroxide to Promote Rechargeable Zinc-Air Battery Performance. *ChemElectroChem* **2020**, *7*, 5005–5012. [[CrossRef](#)]
27. Wang, C.; Zheng, Z.; Chen, Z.; Luo, X.; Hou, B.; Gholizadeh, M.; Gao, X.; Fan, X.; Tan, Z. Enhancement on PrBa_{0.5}Sr_{0.5}Co_{1.5}Fe_{0.5}O₅ Electrocatalyst Performance in the Application of Zn-Air Battery. *Catalysts* **2022**, *12*, 800. [[CrossRef](#)]
28. Bu, Y.; Gwon, O.; Nam, G.; Jang, H.; Kim, S.; Zhong, Q.; Cho, J.; Kim, G. A Highly Efficient and Robust Cation Ordered Perovskite Oxide as a Bifunctional Catalyst for Rechargeable Zinc-Air Batteries. *ACS Nano* **2017**, *11*, 11594–11601. [[CrossRef](#)]
29. Suntivich, J.; Gasteiger, H.A.; Yabuuchi, N.; Nakanishi, H.; Goodenough, J.B.; Shao-Horn, Y. Design Principles for Oxygen-Reduction Activity on Perovskite Oxide Catalysts for Fuel Cells and Metal-Air Batteries. *Nat. Chem.* **2011**, *3*, 546–550. [[CrossRef](#)]
30. Zhu, Z.; Song, Q.; Xia, B.; Jiang, L.; Duan, J.; Chen, S. Perovskite Catalysts for Oxygen Evolution and Reduction Reactions in Zinc-Air Batteries. *Catalysts* **2022**, *12*, 1490. [[CrossRef](#)]

31. Majee, R.; Islam, Q.A.; Bhattacharyya, S. Surface Charge Modulation of Perovskite Oxides at the Crystalline Junction with Layered Double Hydroxide for a Durable Rechargeable Zinc-Air Battery. *ACS Appl. Mater. Interfaces* **2019**, *11*, 35853–35862. [[CrossRef](#)]
32. Peng, S.; Han, X.; Li, L.; Chou, S.; Ji, D.; Huang, H.; Du, Y.; Liu, J.; Ramakrishna, S. Electronic and Defective Engineering of Electrospun CaMnO₃ Nanotubes for Enhanced Oxygen Electrocatalysis in Rechargeable Zinc-Air Batteries. *Adv. Energy Mater.* **2018**, *8*, 1800612. [[CrossRef](#)]
33. Ishihara, T.; Guo, L.M.; Miyano, T.; Inoishi, Y.; Kaneko, K.; Ida, S. Mesoporous La_{0.6}Ca_{0.4}CoO₃ Perovskites with Large Surface Areas as Stable Air Electrodes for Rechargeable Zn-Air Batteries. *J. Mater. Chem. A* **2018**, *6*, 7686–7692. [[CrossRef](#)]
34. Zhang, Y.-Q.; Tao, H.-B.; Chen, Z.; Li, M.; Sun, Y.-F.; Hua, B.; Luo, J.-L. In Situ Grown Cobalt Phosphide (CoP) on Perovskite Nanofibers as an Optimized Trifunctional Electrocatalyst for Zn-Air Batteries and Overall Water Splitting. *J. Mater. Chem. A* **2019**, *7*, 26607–26617. [[CrossRef](#)]
35. Kuai, L.; Kan, E.; Cao, W.; Huttula, M.; Ollikkala, S.; Ahopelto, T.; Honkanen, A.-P.; Huotari, S.; Wang, W.; Geng, B. Mesoporous LaMnO_{3+δ} Perovskite from Spray–Pyrolysis with Superior Performance for Oxygen Reduction Reaction and Zn–Air Battery. *Nano Energy* **2018**, *43*, 81–90. [[CrossRef](#)]
36. Yan, Z.; Sun, H.; Chen, X.; Fu, X.; Chen, C.; Cheng, F.; Chen, J. Rapid Low-Temperature Synthesis of Perovskite/Carbon Nanocomposites as Superior Electrocatalysts for Oxygen Reduction in Zn-Air Batteries. *Nano Res.* **2018**, *11*, 3282–3293. [[CrossRef](#)]
37. Arafat, Y.; Azhar, M.R.; Zhong, Y.; Xu, X.; Tadé, M.O.; Shao, Z. A Porous Nano-Micro-Composite as a High-Performance Bi-Functional Air Electrode with Remarkable Stability for Rechargeable Zinc–Air Batteries. *Nano-Micro Lett.* **2020**, *12*, 130. [[CrossRef](#)]
38. Wang, C.; Hou, B.; Wang, X.; Yu, Z.; Luo, D.; Gholizadeh, M.; Fan, X. High-Performance A-Site Deficient Perovskite Electrocatalyst for Rechargeable Zn–Air Battery. *Catalysts* **2022**, *12*, 703. [[CrossRef](#)]
39. Grimaud, A.; May, K.J.; Carlton, C.E.; Lee, Y.-L.; Risch, M.; Hong, W.T.; Zhou, J.; Shao-Horn, Y. Double Perovskites as a Family of Highly Active Catalysts for Oxygen Evolution in Alkaline Solution. *Nat. Commun.* **2013**, *4*, 2439. [[CrossRef](#)]
40. Kleibeuker, J.E.; Choi, E.-M.; Jones, E.D.; Yu, T.-M.; Sala, B.; MacLaren, B.A.; Kepaptsoglou, D.; Hernandez-Maldonado, D.; Ramasse, Q.M.; Jones, L.; et al. Route to Achieving Perfect B-Site Ordering in Double Perovskite Thin Films. *NPG Asia Mater.* **2017**, *9*, e406. [[CrossRef](#)]
41. Xue, P.; Wu, H.; Lu, Y.; Zhu, X. Recent Progress in Molten Salt Synthesis of Low-Dimensional Perovskite Oxide Nanostructures, Structural Characterization, Properties, and Functional Applications: A Review. *J. Mater. Sci. Technol.* **2018**, *34*, 914–930. [[CrossRef](#)]
42. Tian, Y.; Chen, D.; Jiao, X. La_{1-x}Sr_xMnO₃ (x = 0, 0.3, 0.5, 0.7) Nanoparticles Nearly Freestanding in Water: Preparation and Magnetic Properties. *Chem. Mater.* **2006**, *18*, 6088–6090. [[CrossRef](#)]
43. Li, L.H.; Deng, J.X.; Chen, J.; Xing, X.R. Topochemical Molten Salt Synthesis for Functional Perovskite Compounds. *Chem. Sci.* **2016**, *7*, 855–865. [[CrossRef](#)] [[PubMed](#)]
44. Androulakis, J.; Katsarakis, N.; Giapintzakis, J.; Vouroutzis, N.; Pavlidou, E.; Chrissafis, K.; Polychroniadis, E.K.; Perdikatsis, V. LaSrMnCoO₆: A New Cubic Double Perovskite Oxide. *J. Solid State Chem.* **2003**, *173*, 350–354. [[CrossRef](#)]
45. Tang, T.; Jiang, W.-J.; Liu, X.-Z.; Deng, J.; Niu, S.; Wang, B.; Jin, S.-F.; Zhang, Q.; Gu, L.; Hu, J.-S.; et al. Metastable Rock Salt Oxide-Mediated Synthesis of High-Density Dual-Protected M@NC for Long-Life Rechargeable Zinc–Air Batteries with Record Power Density. *J. Am. Chem. Soc.* **2020**, *142*, 7116–7127. [[CrossRef](#)]
46. Chen, C.-F.; King, G.; Dickerson, R.M.; Papin, P.A.; Gupta, S.; Kellogg, W.R.; Wu, G. Oxygen-Deficient BaTiO_{3-x} Perovskite as an Efficient Bifunctional Oxygen Electrocatalyst. *Nano Energy* **2015**, *13*, 423–432. [[CrossRef](#)]
47. Bao, J.; Zhang, X.; Fan, B.; Zhang, J.; Zhou, M.; Yang, W.; Hu, X.; Wang, H.; Pan, B.; Xie, Y. Ultrathin Spinel-Structured Nanosheets Rich in Oxygen Deficiencies for Enhanced Electrocatalytic Water Oxidation. *Angew. Chem. Int. Ed.* **2015**, *54*, 7399–7404. [[CrossRef](#)]
48. Ji, Q.; Bi, L.; Zhang, J.; Cao, H.; Zhao, X.S. The Role of Oxygen Vacancies of ABO₃ Perovskite Oxides in the Oxygen Reduction Reaction. *Energy Environ. Sci.* **2020**, *13*, 1408–1428. [[CrossRef](#)]
49. She, S.; Yu, J.; Tang, W.; Zhu, Y.; Chen, Y.; Sunarso, J.; Zhou, W.; Shao, Z. Systematic Study of Oxygen Evolution Activity and Stability on La_{1-x}Sr_xFeO_{3-δ} Perovskite Electrocatalysts in Alkaline Media. *ACS Appl. Mater. Interfaces* **2018**, *10*, 11715–11721. [[CrossRef](#)]
50. Yu, J.; Sunarso, J.; Zhu, Y.; Xu, X.; Ran, R.; Zhou, W.; Shao, Z. Activity and Stability of Ruddlesden–Popper-Type La_{n+1}Ni_nO_{3n+1} (n = 1, 2, 3, and ∞) Electrocatalysts for Oxygen Reduction and Evolution Reactions in Alkaline Media. *Chem. Eur. J. Chem.* **2016**, *22*, 2719–2727. [[CrossRef](#)]
51. Zhu, Y.; Zhou, W.; Zhong, Y.; Bu, Y.; Chen, X.; Zhong, Q.; Liu, M.; Shao, Z. A Perovskite Nanorod as Bifunctional Electrocatalyst for Overall Water Splitting. *Adv. Energy Mater.* **2017**, *7*, 1602122. [[CrossRef](#)]
52. Merino, N.A.; Barbero, B.P.; Eloy, P.; Cadús, L.E. La_{1-x}Ca_xCoO₃ Perovskite-Type Oxides: Identification of the Surface Oxygen Species by XPS. *Appl. Surf. Sci.* **2006**, *253*, 1489–1493. [[CrossRef](#)]
53. Zhong, Y.; Xu, X.; Liu, P.; Ran, R.; Jiang, S.P.; Wu, H.; Shao, Z. A Function-Separated Design of Electrode for Realizing High-Performance Hybrid Zinc Battery. *Adv. Energy Mater.* **2020**, *10*, 2002992. [[CrossRef](#)]
54. Kim, H.-I.; Kim, E.-J.; Kim, S.-J.; Shin, H.-C. Influence of ZnO Precipitation on the Cycling Stability of Rechargeable Zn–Air Batteries. *J. Appl. Electrochem.* **2015**, *45*, 335–342. [[CrossRef](#)]
55. Lee, J.-S.; Kim, S.T.; Cao, R.; Choi, N.-S.; Liu, M.; Lee, K.T.; Cho, J. Metal-Air Batteries with High Energy Density: Li-Air versus Zn-Air. *Adv. Energy Mater.* **2011**, *1*, 34–50. [[CrossRef](#)]

56. Miao, H.; Wang, Z.; Wang, Q.; Sun, S.; Xue, Y.; Wang, F.; Zhao, J.; Liu, Z.; Yuan, J. A New Family of Mn-Based Perovskite ($\text{La}_{1-x}\text{Y}_x\text{MnO}_3$) with Improved Oxygen Electrocatalytic Activity for Metal-Air Batteries. *Energy* **2018**, *154*, 561–570. [[CrossRef](#)]
57. Seong, A.; Kim, J.; Kwon, O.; Jeong, H.Y.; Gorte, R.J.; Vohs, J.M.; Kim, G. Self-Reconstructed Interlayer Derived by In-Situ Mn Diffusion from $\text{La}_{0.5}\text{Sr}_{0.5}\text{MnO}_3$ via Atomic Layer Deposition for an Efficient Bi-Functional Electrocatalyst. *Nano Energy* **2020**, *71*, 104564. [[CrossRef](#)]

Disclaimer/Publisher's Note: The statements, opinions and data contained in all publications are solely those of the individual author(s) and contributor(s) and not of MDPI and/or the editor(s). MDPI and/or the editor(s) disclaim responsibility for any injury to people or property resulting from any ideas, methods, instructions or products referred to in the content.